Development of a multifunctional nanoindenter integrated in-situ Scanning Electron Microscope - application to the monitoring of piezoresponse and electro-mechanical failures

F. Volpi, C. Boujrouf, M. Rusinowicz, S. Comby-Dassonneville, F. Mercier, R. Boichot, M. Chubarov, Rosine Coq Germanicus, F. Charlot, M. Braccini, et al.

Development of a multifunctional nanoindenter integrated in-situ Scanning Electron Microscope - Application to the monitoring of piezoresponse and electro-mechanical failures

F. Volpi [a*], C. Boujrouf [a], M. Rusinowicz [a], S. Comby-Dassonneville [a], F. Mercier [a], R. Boichot [a], M. Chubarov [a], R. Coq Germanicus [b], F. Charlot [c], M. Braccini [a], G. Parry [a], D. Pellerin [d], M. Verdier [a]

[a] Univ. Grenoble Alpes, CNRS, Grenoble INP, SIMaP, 38000 Grenoble, France

[b] Normandie Univ. ENSICAEN, UNICAEN, CNRS, CRISMAT, 14000 Caen, France

[c] Univ. Grenoble Alpes, CNRS, Grenoble INP, CMTC, 38000 Grenoble, France

[d] Scientec / CSInstruments, 91940 Les Ulis, France

Corresponding author: fabien.volpi@grenoble-inp.fr

Abstract

The rising complexity of multi-material structures integrated into multi-functional devices requires the development of dedicated characterization tools capable of simultaneously monitoring different physical magnitudes with a relevant spatial resolution. This paper reports the development and the application of an original instrument based on a nanoindenter coupled with fine electrical measurements and integrated in-situ a Scanning Electron Microscope (SEM). The performances and capabilities of this home-developed instrument are illustrated through two different case studies.

First, a micrometer-scale piezoelectric structure made up of wurtzite-single crystalline AlN islands grown on top of conductive Si pillars is tested. In-situ SEM imaging is used to precisely position the indenting probe on these individual islands, while the instrument sensitivity and repeatability are used to monitor their low-signal piezoresponse. Effective piezoelectric coefficients are also extracted for different loading/unloading conditions.

Secondly a Si_3N_4/AlSiCu/SiO_2 stack, which is standardly integrated as a passivation structure on top of microelectronic chips, is electrically and mechanically stressed and monitored up to its failure. The mechanical failure mechanisms (buried or emerging cracks) are discriminated thanks to the real-time SEM imaging of the indentation test. The instrument high sensitivity is used to monitor early current leakages that are attributed to conduction paths induced by mechanical failures.

Combining high electro-mechanical sensitivity and precise probe positioning appears as an efficient way to monitor and analyze low-level electrical responses of small-scale structures. This approach paves the way to the fine characterization of micro/nano-systems displaying

mechanically-driven electrical properties (conduction mechanism, leakage, breakdown,…) like 2D-materials, dielectrics in microelectronic devices, strain-sensors, enamelled Litz wires,…

Keywords

Nanoindentation; Scanning electron microscopy, In-situ measurements; Electro-mechanical properties; Piezoelectric properties, Failure

1. Introduction

Whether addressing microelectronics, sensors, imagers, power sourcing or power storage, the complexity of small-scale devices has never stopped rising since the early ages of microelectronics. This rising complexity has required the integration of ever more heterogeneous multi-layer structures that combine different material families (semiconductors, dielectrics, metals) with dissimilar properties: ductility vs brittleness for mechanical properties, conductivity vs dielectric behavior for electrical properties, opacity vs transparency for optical properties,… Because of these spatial and functional heterogeneities, some dedicated characterization tools should be developed to monitor simultaneously various physical magnitudes with relevant spatial resolutions.

Nanoindentation is a well-known technique dedicated to the local and quantitative mechanical testing of materials at nanoscales [1-2]. Numerous developments have been made to expand the capabilities of this technique [3]: real-time imaging in Scanning Electron Microscopes (SEM) [4-5] or in Transmission Electron Microscopes (TEM) [6-8], high temperature nanoindentation [9-11], coupling with electrochemical analysis [12], coupling with electrical measurements,... The latter development (usually referred to as ‘nano-ECR’ or ‘resistive-nanoindentation’) was driven by a wide spectrum of motivations such as the local monitoring of phase transformation [13-19], the study of native oxide fractures [20-22], the characterization of piezoelectric materials [23-24], the investigation of microsystem operation [25], the monitoring of dielectric film behaviors [26-27] and the contact area computation during nanoindentation tests [28-33]. Beyond the instrumental development, a challenging step of this electro-mechanical coupling remains the quantitative processing of raw data [26,30,34,35]. As already stated, the real-time imaging of nanoindentation tests has been widely reported, but only few attempts have been

made to combine electrical measurements and real-time observations in-situ SEM: for the electro-mechanical characterization of graphene in a dedicated device (nanoindenter was then used for mechanical actuation only) [36], for post-mortem observations of indentation imprints [37] or for the local characterization of multi-phased alloys [38].

The present article reports the development of a home-developed nanoindenter functionalized for highly-sensitive electrical measurements and integrated in-situ SEM. In order to highlight its sensing and positioning capabilities, this instrument is employed to characterize two different multi-material structures involving dielectric thin films. First the piezoelectric response of a micrometer-scale structure made up of aluminum nitride (AlN) islands grown on top of silicon (Si) pillars is measured. Secondly, the behavior of a Si_3N_4/AlSiCu stack is monitored up to its electrical and mechanical failures and correlated to the real-time SEM imaging of the indent.

2. Experimental details

2.1. Electrically-functionalized and SEM-integrated nanoindenter

The experimental set-up combines different commercial instruments with customized adapter systems. Fig. 1 and 2 present a scheme and an infra-red view of the set-up once integrated within the SEM chamber. The nanoindentation head is a commercial actuator (InForce 50 actuator from Nanomechanics Inc / KLA-Tencor), displaying a maximum load of 50 mN and a static load resolution below 0.1 µN. This force-controlled actuator enables continuous stiffness measurement (CSM) that gives access to the continuous extraction of both hardness and elastic modulus. All the experiments presented in this paper have been performed with boron-doped diamond tips with resistivity in the range of [0.2-2] Ω.cm (with either cube-corner or flat-punch shapes) supplied by Synton-MDP. The whole electrical measurement chain is fully guarded up to the tip: a guard ring is patterned on a ceramic element that insulates the tip from the grounded metallic extender (see inset in Fig. 2). Electrical contacts to the tip and guard ring are made with 50-µm large copper wires connected to fixed plugs. The circuit leakage is low (in the fA range) and constant, which makes it possible to null this offset by simple subtraction. The set-up shielding leads to a noise RMS-amplitude circa 3 fA. The Actuator and sample displacements are performed with linear positioners from SmarAct GmbH. Typical travel ranges are at the cm-scale with a ~1 nm resolution.

Different electrical magnitudes can be measured with this set-up: leakage current, quasi-static resistance, dielectric capacitance, piezoresponse,… In the present case, focus is made on piezoresponse and electrical conduction. Current measures were conducted with highly-sensitive ammeter or electrometer: 6430 model from Keithley (allowing current sensitivity as

low as the fA range) or 6514 model from Keithley, respectively. Resistance measures were performed with a ResiScope apparatus from CSI/Scientec. Originally developed for conductive-atomic force microscopy [39], this device is optimized for real-time and self-compliant resistance measurements. It ranges from 100 Ω to 1 TΩ, with acquisition rates up to 1kHz.

The overall set-up has been designed to be integrated into an SEM. In the present work, the SEM apparatus used was a Field Emission Gun Gemini SEM 500 from Carl Zeiss. In standard conditions, the specimen surface was scanned under a 60° tilt angle. SEM-integration allows positioning of indents with a precision better than 100nm [38]. Electrical-nanoindentation experiments can be performed either ex-situ or in-situ SEM.

2.2. Samples

Two dielectric structures displaying drastically different mechanical and electrical behaviors are characterized in the present work.

Sample 1 is made up of micro-scale wurtzite-single crystalline AlN islands grown on top of conductive Si pillars. AlN islands were grown from chlorinated precursors and ammonia, $AlCl_3/NH_3$ diluted in N_2 and H_2. Patterned Si substrates were home-made from p-type boron doped single side epi-ready polished Si (111) wafers. A 5 to 10 nm buffer layer of SiC was in situ synthesized prior to the growth of AlN. In order to promote local growth of AlN only on top of Si pillars, heteroepitaxial growth has been conducted at $1.5\ 10^4$ Pa pressure with high concentration of the precursors in the gas phase. Additional details are given in [40]. Structural investigation with TEM and Raman spectroscopy reveal a lower defect density and reduction of stress in AlN locally grown on pillar compared to AlN grown on Si flat substrate. Due to the

patterning technique and the photoresist mask used, hexagonal pillars (as presented in [40]) and rhombus pillars can be obtained simultaneously at different locations on the same wafer. In the present work, we report on the piezoelectric behavior of AlN islands grown on rhombus pillars since in-depth structural characterization by X-Ray diffraction techniques and transmission electron microscopy observations does not reveal noticeable differences for AlN islands grown on both type of pillars (not presented here). Si pillars were typically 20-30 µm high and ~5 µm wide.

Sample 2 is a stack of dielectric and metallic alloy films. The topmost layer is a Si_3N_4 film usually integrated at the end of manufacturing process to protect microelectronic chips from the ambient moisture and contaminants [41-42]. Beyond these chemical requirements, this layer must withstand the mechanical stresses that develop during packaging processes (grinding, dicing, bumping, ball dropping, cleaving or sawing) [43-44]. These processes can nucleate and propagate cracks inside the multi-layer stacks that degrade chip integrity [45]. Preventing these stress-induced failures requires to properly apprehend the electro-mechanical behavior of these multi-material stacks. Sample 2 consists of a 450 nm-thick SiO_2 layer deposited by Plasma Enhanced Chemical Vapor Deposition (PECVD), covered by a sputtered 3µm-thick $Al_{98.96}Si_{1.00}Cu_{0.04}$ (AlSiCu) film, and covered by a 1.3 µm-thick Si_3N_4 layer (grown by PECVD at ~400 °C with a SiH_4/NH_3 gas mixture). The stack was grown on a (001)-oriented silicon wafer.

2.3. Residual imprint characterizations

Residual nanoindentation imprints were essentially observed by SEM. Top-surface views were taken with the same SEM as the one used for in-situ experiments (Gemini SEM 500 from Carl

Zeiss). Cross-views were taken after focused ion-beam (FIB) milling, using a FIB Cross Beam NVision 40 from Carl Zeiss (Ga source with an acceleration voltage of 30 kV and current intensity of 300 pA).

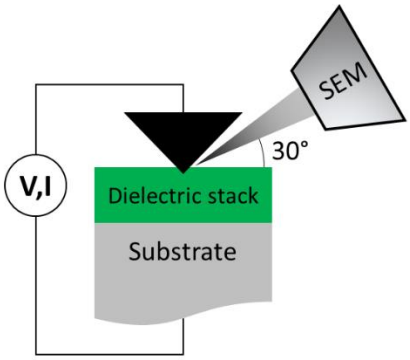

Fig. 1. Scheme of the resistive-nanoindentation set-up in the "in-situ SEM" configuration.

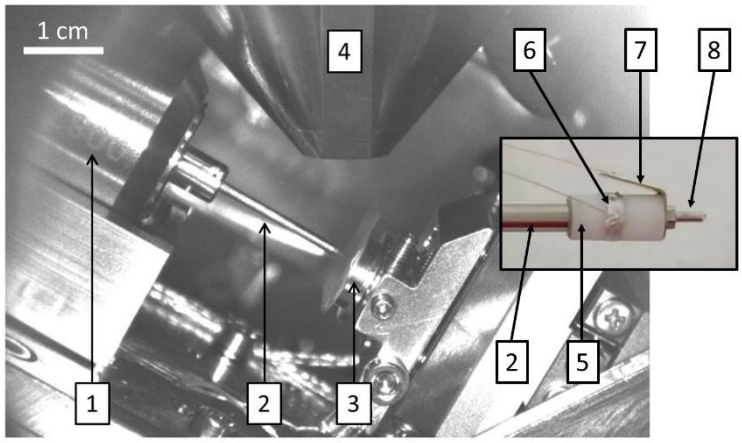

Fig. 2. Infra-Red view of the set-up once integrated within the SEM. A close-up on tip connections is shown in inset. 1 = Nanoindenter head, 2 = Extender, 3 = Specimen, 4 = SEM column, 5 = Ceramic element, 6 = Guard terminal, 7 = Signal terminal, 8 = Tip.

3. Results and discussion

3.1. Characterization of micrometer-scale piezoelectric AlN islands

As they combine both mechanical and electrical stimuli, electrically-functionalized nanoindenters are particularly well suited for the characterization of piezoelectric materials [24,46], as a complementary approach to Piezoresponse Force Microscopy technique (PFM) [47-48]. Pioneering works on bulk piezoelectric materials [49] or on thin films have shown the possibility to perform quantitative measures of direct [50] or converse piezoelectric effects [23], as well as depolarization phenomena in ferroelectric materials [51]. The testing of nanostructured samples (piezoelectric nano-islands, nano-rods,…) has also been reported [34,52]: the indenter positioning was then either performed by running the instrument in a "piezo scanning mode" where the indenter senses the surface in a try-error process [34], or after topography characterization by scanning probe microscopy [52]. These pioneering works highlight the challenge of probe positioning in piezoresponse testing with nanoindenters. However, beyond these achievements, the reported positioning procedures may present different drawbacks. For instance, they cannot apply when the sample has a flat surface (i.e. when the domain to be indented has no relief). Moreover, in the case of "piezo scanning mode", the procedure might induce surface damages on sensitive samples. We hereafter present a case study where in-situ SEM-monitoring appears as an alternative solution for direct spatial positioning. More generally, this case study illustrates the capability of the present instrument to perform quantitative direct piezoelectric measures at ultra-low electrical level with appropriate spatial resolution.

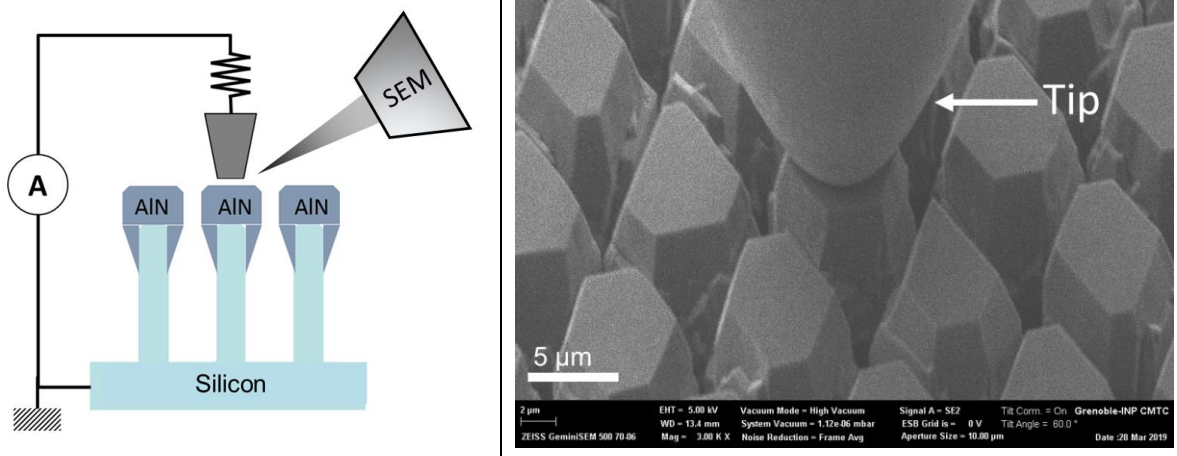

Fig. 3. (a) Schematic of the overall set-up for the characterization of sample 1 (b) SEM-view of sample 1 under test (Acc. Voltage = 5 kV).

3.1.1. Testing procedure

Fig. 3a shows a schematic of the overall set-up for the piezoresponse monitoring of Sample 1 under SEM observation. Si pillars were taken as electrical back-contacts to the AlN islands and were grounded, while the indenter tip was taken as both the mechanical strainer and the electrical front-side contact. In order to apply a homogeneous mechanical strain onto islands, a flat-punch geometry was chosen for the indenter tip (5 µm of diameter). A typical SEM-view of the flat-punch tip in contact with an AlN island is shown in Fig. 3b. Because of unavoidable misalignments of the workpieces constituting the experimental set-up, an intrinsic angular misalignment builds-up between the flat-punch and specimen surfaces. This angle has been measured experimentally on this set-up to be circa 0.01 rad, which is rather standard for nanoindentation systems [53]. In order to ensure the flat-punch to be fully in contact with the sample surface all along the test, an initial mechanical load of 10 mN was applied before piezoelectric testing. For the present experiments, choice has been made to monitor the current

flowing through the tip rather than voltage changes. Electrometer was then set on its ammeter mode with 0 V applied to the tip (thus ensuring the zero-field condition).

3.1.2. Piezoelectric response measurements

The piezoresponse of the AlN islands was assessed through load cycles performed by steps of 10 mN. A typical load-displacement curve showing the reversible mechanical behavior of the structure over three successive cycles is shown in Fig. 4. An example of load and current data monitored during one of these load cycles is given in Fig. 5a. Current bursts are clearly observed for each load step (increment/decrement). Compressive forces result in positive current peaks and the return to equilibrium produces a negative current. The amplitude of the return peaks is almost twice weaker. The ultra-low current level (several tens of fA) is orders of magnitude lower than standardly reported in literature [34,49,54]. This lower level can be explained by the combination of both intrinsic and geometrical attributes: 1/ AlN has a much lower intrinsic piezoelectric response than perovskite-like structures often reported in literature (~5 vs 100-1000 pC/N, respectively) [24,55] and 2/ the contact radius (only 5 µm wide in the present work) scales one or two orders of magnitude lower than typical contact radiuses obtained with large spherical tips. The measurement repeatability can be observed in Fig. 5b, where load cycles clearly superimpose despite the very low signal. Then the amount of generated charges has been obtained by integrating current curves. The order of magnitude for each charge burst is several tens of fC. An effective piezoelectric coefficient d_{eff} can then be extracted for each load step (increment/decrement) by calculating the ratio between generated charges and load step amplitude [50]. As load changes were performed at a constant strain rate of 0.5 %/s, various load rates were assessed from a step to another (from ~7 to ~16 mN/s). The dependence of the

effective piezoelectric coefficient d_{eff} against this load rate, calculated for each load step (increment/decrement) is shown in Fig. 6. These values are in full agreement with reported data on AlN thin films [56-57]. It is to be noted that d_{eff} depends on the loading direction (loading vs unloading) and on load rate. The dependence on load rate is usually observed on ferroelectric materials where depolarization kinetics modify the overall response [34,50-51] and thus requires dedicated experiments [34]. The lower value measured during unloading (up to 50% difference) can be attributed to a polarization effect, as observed by PFM on polycrystalline AlN [57]. This point is in accordance with the spontaneous polarization expected on these single crystalline AlN islands [58]. In order to make sure without ambiguity of the piezoelectric origin of this signal, the same procedure has been applied to an amorphous silica film, that generated no electrical signal.

To conclude on this part, the in-situ SEM imaging was shown to enable the precise positioning of the indenting probe on a micro-scale piezoelectric structures. The instrument high sensitivity and repeatability, essentially due to the fully-guarded measurement chain, are used to monitor and quantitatively analyze low-signal piezoresponse. These performances open the way to the testing of materials with moderate piezoresponse (like III-V and II-VI semiconductors [59-60]) and/or small-scale structures (like piezoelectric scaffold nanostructures [61-62]) that would be difficult to sense otherwise.

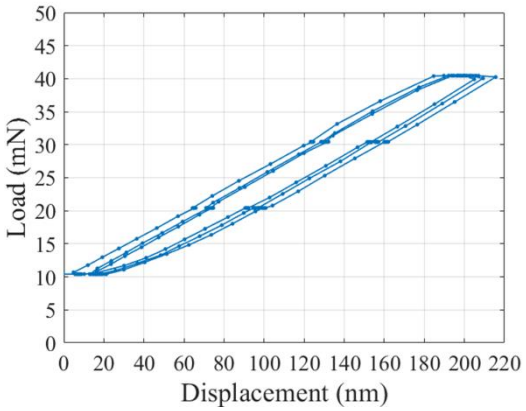

Fig. 4. Load-displacement curves over three successive stress cycles.

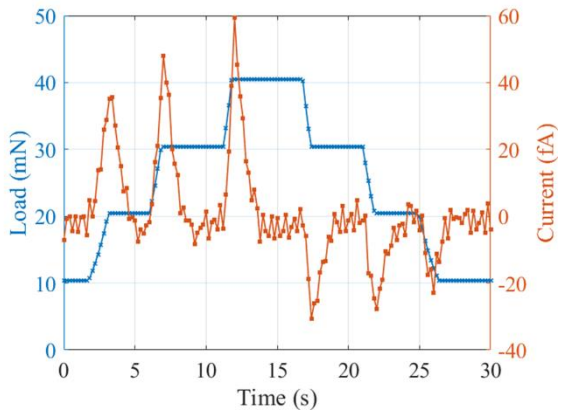

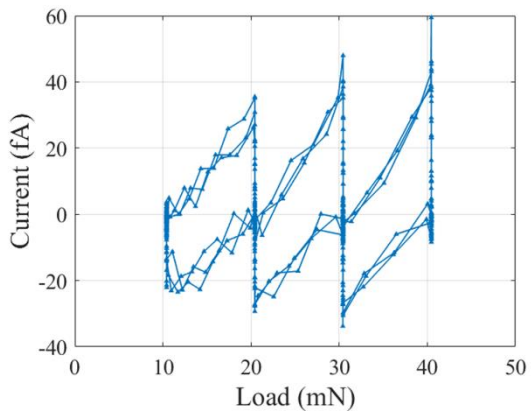

Fig. 5. (a) Current and load vs time over one stress cycle. (b) Current vs load over three successive stress-cycles.

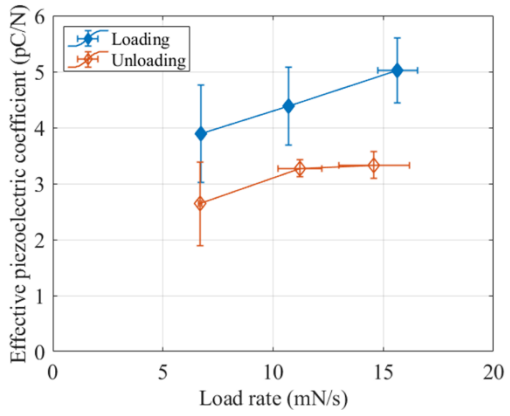

Fig. 6. Effective piezoelectric coefficient against loading/unloading rate. Error bars were calculated from the dispersion on the three successive loading/unloading cycles shown in Fig.4.

3.2. Electro-mechanical behaviors and failures of a dielectric/metal stack

In advanced semiconductor manufacturing, integrated structures can be subjected to large mechanical stresses during processing (during the Chemical Mechanical Polishing process step for instance [63]), during packaging (wafer grinding, dicing, cleaving or sawing processes [43-44]) or even during operation [64-66]. These stresses may lead to both electrical and/or mechanical failures: electrical leakage, electrical breakdown, cracks,… Preventing these stress-induced failures first requires to properly apprehend the mechanical behavior of these multi-material stacks. In that purpose, a tool able to both actuate and sense these phenomena under real-time imaging should allow a better description of device reliability.

3.2.1. Testing procedure

Fig. 7 shows a schematic of the overall set-up for the testing of Sample 2. Resistive-nanoindentation tests were performed in-situ SEM with a cube-corner tip under 10 V. The cube-corner shape was chosen for two reasons. Firstly, it allows a large field of view of the indented area under the 60° tilted beam incidence in SEM. Secondly, it allows to scan a larger range of mechanical deformations than a Berkovich shape. When idents were performed under SEM imaging, the electrical response was measured with the Resicope module. For the monitoring of ultra-low currents, SEM imaging was switched off and measures were performed with a Keithley 6430 module.

3.2.2. Electro-mechanical monitoring

Fig. 8 reports the mechanical and electrical responses of a typical indent performed in-situ SEM, while current was recorded with the Resiscope module. For this experiment, the final load was 45 mN, leading to a penetration depth of ~3.5 µm. From the mechanical point of view, various pop-in events are recorded all along indentation. The first pop-in is observed at 529 nm (~100 nm long), while the largest one spans from 1454 nm to 1980 nm (more than 500 nm long). Such pop-in events have been widely reported in literature [67-69] and attributed to interfacial delamination, and/or to film cracking [69-70]. In order to discriminate these phenomena, indentation tests have been fully recorded in video format. Several snapshots have been extracted at characteristic points of the indentation curve. Fig. 9 reports the SEM views corresponding to the four marks on the loading curve (pictures were taken right after each pop-in event). Two significant points are highlighted: 1/ the three first pop-ins (marks A, B and C) do not lead to crack emerging at the free surface of the Si_3N_4 film and 2/ the largest pop-in (mark D) corresponds to the appearance of an orthoradial crack circumventing the indenting area (pointed in the figure). Generally, pop-in events can be the signature of different phenomena such as the nucleation of dislocations [71], stressed-induced phase transformation [72], twinning [73] or film cracking [67,74]. The great acuity of cube-corner tips is known to initiate early mechanical cracks underneath and around the indenter [67,75-77]. Consequently, in the present case, the first pop-ins (marks A, B and C) can be attributed to cracks that initiate and propagate inside the Si_3N_4 film, between the tip and the underlying AlSiCu ductile film. The development of these cracks is expected to generate high densities of electrical defects that tend to shortcut these two electrodes (tip and AlSiCu film). On the contrary, the D pop-in corresponds to a crack that initiates at the free surface of the Si_3N_4 layer and then propagates

within the layer, thus leading to the visible orthoradial crack. For this crack, the corresponding electrical defects do not shortcut the two electrodes.

From the electrical point of view, leakage current remains at the Resiscope ground level (several tens of pA) from 0 to 2700 nm before a steep current rise. This noise around ground level is due to electron injection into the tip by the SEM beam during real-time imaging. The inset of Fig. 8 shows the current monitored during the first 10 seconds of the test, thus highlighting periodical current bursts due to beam scanning. This point appears as the most important limitation to real-time SEM imaging of resistive-nanoindentation on dielectric structures, as it prevents current measures below the pA level. Even though this threshold can be lowered by optimizing the observation conditions, it remains an inevitable limitation. However, it is to be noted that the characterization of conductive or leaky systems (metallic alloys [38], strain sensors [78], microelectronic-integrated dielectrics [79-80]...) is not or weakly affected by this issue as long as the relevant signal exceeds this pA level. Finally, the steep current rise at 2700 nm reaches hundreds of µA before smoothly increasing until final loading.

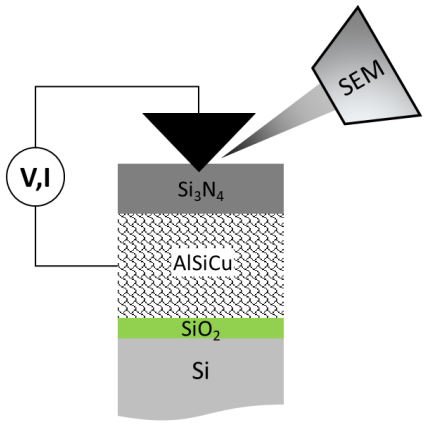

Fig. 7. Schematic set-up for the characterization of sample 2.

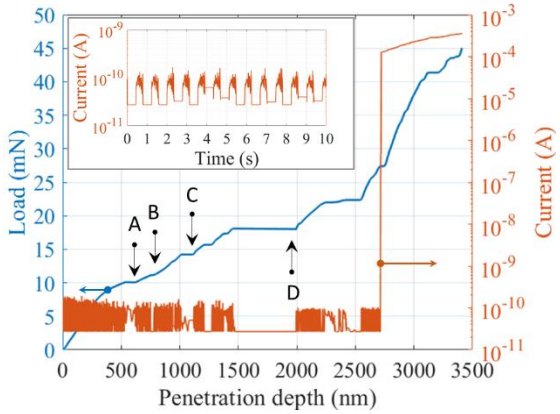

Fig. 8. Resistive-nanoindentation tests on sample 2 performed in-situ SEM with Resiscope module (SEM imaging turned on). The current monitored during the first 10 seconds of the test are shown in inset.

The correlation of these mechanical and electrical failures can then be discussed. It appears that the steep current rise at 2700 nm occurs far after numerous cracks within the dielectric. In order to explain this current rise, residual imprints have been FIB-sliced and observed by SEM. Fig. 10 shows the indent imprint before and after FIB-slicing. In Fig. 10b, the Si_3N_4/AlSiCu interfaces have been delineated with dashed lines in order to identify the position of the tip at the final stages of indentation. It can be seen that the tip apex has reached the AlSiCu layer lately during indentation. As the gap between the Si_3N_4 crack edges (pointed with dashed arrows) is filled by AlSiCu, it can be concluded that the steep current rise at 2700 nm was an electrical shortcut between the tip and the AlSiCu layer, and this shortcut was consecutive to the creep extrusion of AlSiCu through the Si_3N_4 crack. This point is in agreement with the smooth current increase observed after this electrical shortcut: AlSiCu extrusion further extends under the ongoing indentation.

In order to better follow the evolution of current flowing through the dielectric film before this failure, another experiment run with the 6430 module from Keithley has been carried-out (Fig. 11). In this very case, SEM imaging was turned off to avoid current overflow induced by electron injection. A similar steep current rise (still associated to the direct tip/metal contact) is also observed at large penetration depth, but it can be seen that the Si_3N_4 dielectric film actually starts leaking at much smaller depths: leakage currents are detectable short after the first pop-in (800 nm for this test) and increase continuously up to the final electrical shortcut. This leakage increase during indentation is attributed to the generation of electrical defects along crack side-walls that form conduction paths. The slight current overshoots observed after each mechanical pop-in are inductive currents generated by the corresponding abrupt tip motions. Correspondences between mechanical pop-ins and current bursts are pointed with dashed lines. From test to test, slight differences in pop-in frequency, incursion amplitude,… can be observed (compare loading curves of Fig. 8 and 11). These differences are mainly driven by the microstructure of the underlying films (the highest acuity of the cube-corner tip makes it more sensitive than Berkovich tips to local heterogeneities).

As a conclusion on the characterization of this stack, the high sensitivity of the set-up is used to monitor both electrical and mechanical failures: early leakages are detected and related to conduction paths induced by mechanical failures. Real-time SEM imaging has allowed to discriminate the type of mechanical failure mechanisms (buried and/or emerging cracks) correlated with load-displacement curves. This case study shows that the present instrument would be an efficient tool to characterize materials displaying mechanically-driven conduction mechanisms: 2D-materials (carbon-based materials, MoS_2, Ag-nanowire networks,…) [36,81-83], materials for strain-sensors or flexible electronics [78,84], dielectrics in microelectronic

devices (leakage and failure of low-permittivity dielectrics subjected to mechanical stresses) [79-80,85], enamel coatings [86],… In these cases, real-time SEM observation would be used either for probe positioning or for the monitoring of failure.

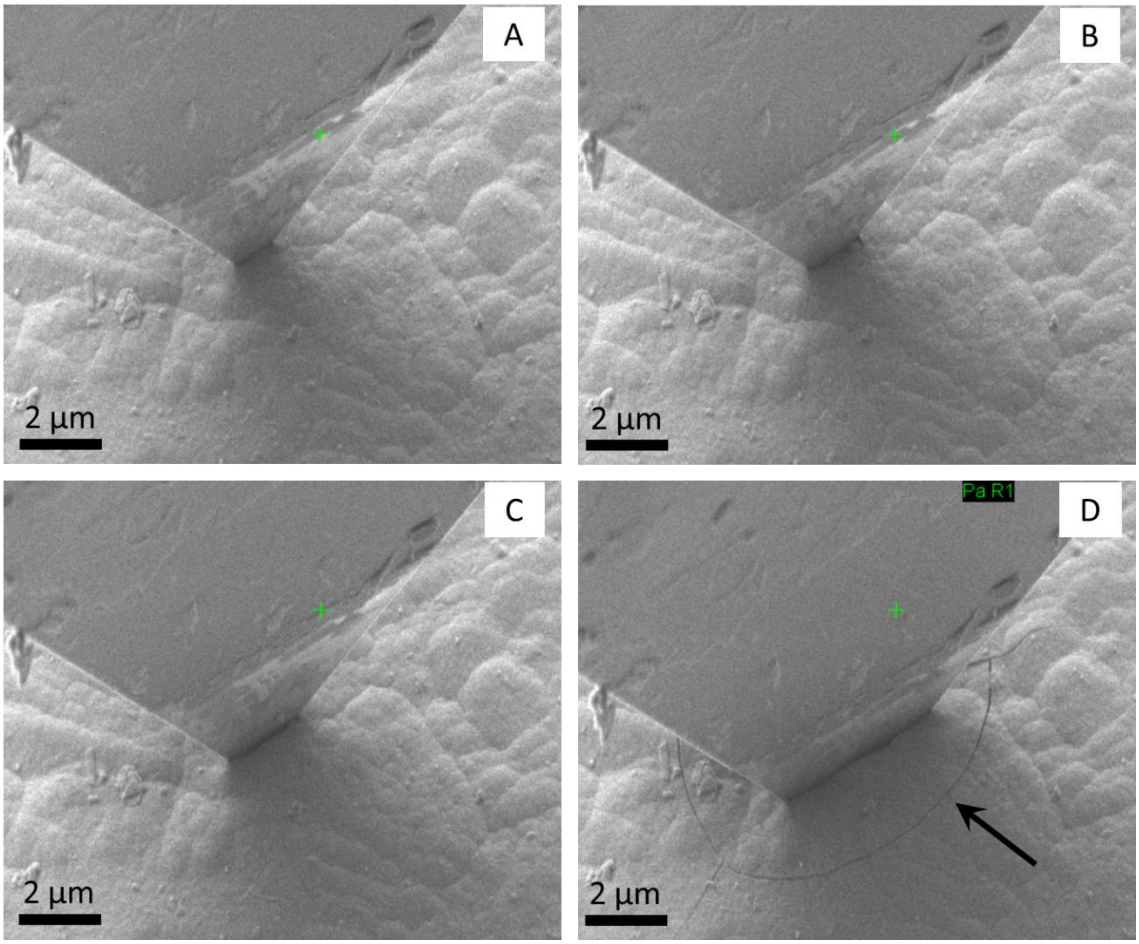

Fig. 9. Snapshots of in-situ SEM resistive-nanoindentation tests. The figure labels refer to the pop-in marks in Fig. 8. (Acc. Voltage = 2 kV)

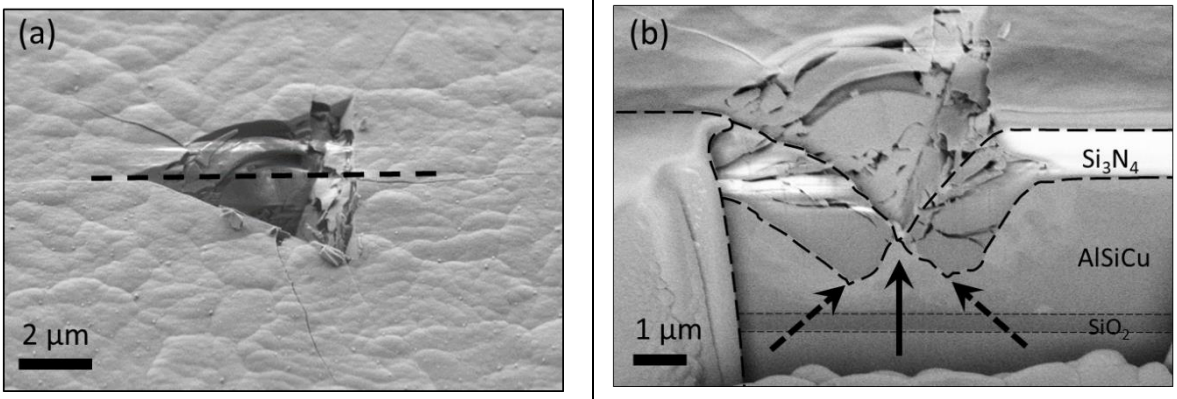

Fig. 10. SEM observations of residual imprints on stack 2. (a) Before FIB-slicing. Dashed line delineates the FIB-slicing position (b) After FIB-slicing. Si_3N_4/AlSiCu interfaces are delineated with dashed lines. Edges of the Si_3N_4 cracks are pointed with dashed arrows. AlSiCu extrusion through the Si_3N_4 film is pointed with full arrow.

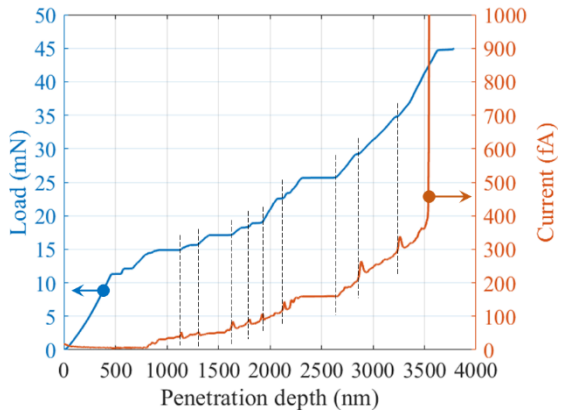

Fig. 11. Resistive-nanoindentation test performed on sample 2 with Keithley 6430 module (SEM imaging turned off).

4. Conclusion

The present paper reports the technical description and application of a home-developed characterization device based on a nanoindenter. The nanoindenter has been functionalized to perform electrical measurements and adapted to be integrated in-situ SEM. In order to highlight its performances, this instrument is applied to the fine characterization of two different multi-material structures involving dielectric thin films. The guarded electrical measurement chain is shown to enable highly sensitive measures: low-level signals (down to tens of fA) of both piezoresponse and leakage currents have been monitored and related to mechanical events (elastic strain and cracks, respectively). This high sensitivity is particularly interesting for the characterization of functional thin films where low-level leakage currents are most common. For instance, this instrument opens the way to the monitoring of electrical conduction and failure mechanisms induced by mechanical stresses on dielectrics in microelectronic devices (like high- or low-permittivity dielectrics that are subjected to thermo-mechanical stress cycles), on passivation enamels of Litz wires (these coatings are subjected to harsh mechanical wear all along their lifetime),… Real-time SEM imaging enables the precise positioning of the probe on micro-scale structures, as well as the discrimination of mechanical failure mechanisms. The variety of these case studies illustrates the versatility of this instrument, as well as its potential for further developments and applications.

5. Acknowledgments

This work has been performed with the financial support of the Centre of Excellence of Multifunctional Architectured Materials "CEMAM" n° ANR-10-LABX-44-01. The CEMAM program is funded by the French Agence Nationale de la Recherche (ANR).

The authors thank the technical team of SIMaP lab (B. Mallery, S. Massucci and N. Vidal) for its support, as well as members of CSI/Scientec company (Les Ulis, France) for their support for the functionalization of the nanoindentation head: L. Pacheco, A. Lecoguiec and S. Poulet.

The authors would like to thank F. Lallemand et M. Choquet from Murata Caen for the design and fabrication of the Si_3N_4/AlSiCu/SiO_2 sample.

6. References

[1] J.B. Pethica, R. Hutchings, W.C. Oliver, Composition and hardness profiles in ion implanted metals, Nucl. Instrum. Methods Phys. Res. 209–210 (1983) 995–1000. https://doi.org/10.1016/0167-5087(83)90911-0.

[2] J.L. Loubet, J.M. Georges, O. Marchesini, G. Meille, Vickers Indentation Curves of Magnesium Oxide (MgO), J. Tribol. 106 (1984) 43–48. https://doi.org/10.1115/1.3260865.

[3] H. Nili, K. Kalantar-zadeh, M. Bhaskaran, S. Sriram, In situ nanoindentation: Probing nanoscale multifunctionality, Prog. Mater. Sci. 58 (2013) 1–29. https://doi.org/10.1016/j.pmatsci.2012.08.001.

[4] R. Rabe, J.-M. Breguet, P. Schwaller, S. Stauss, F.-J. Haug, J. Patscheider, J. Michler, Observation of fracture and plastic deformation during indentation and scratching inside the scanning electron microscope, Thin Solid Films. 469–470 (2004) 206–213. https://doi.org/10.1016/j.tsf.2004.08.096.

[5] J.D. Nowak, K.A. Rzepiejewska-Malyska, R.C. Major, O.L. Warren, J. Michler, In-situ nanoindentation in the SEM, Mater. Today. 12 (2010) 44–45. https://doi.org/10.1016/S1369-7021(10)70144-9.

[6] M.A. Wall, U. Dahmen, An in situ nanoindentation specimen holder for a high voltage transmission electron microscope, Microsc. Res. Tech. 42 (1998) 248–254. https://doi.org/10.1002/(SICI)1097-0029(19980915)42:4<248::AID-JEMT3>3.0.CO;2-M.

[7] A.M. Minor, E.T. Lilleodden, E.A. Stach, J.W. Morris, In-situ transmission electron microscopy study of the nanoindentation behavior of Al, J. Electron. Mater. 31 (2002) 958–964. https://doi.org/10.1007/s11664-002-0028-4.

[8] A. Nafari, J. Angenete, K. Svensson, A. Sanz-Velasco, P. Enoksson, MEMS sensor for in situ TEM-nanoindentation with simultaneous force and current measurements, J. Micromech. Microeng. 20 (2010) 064017. https://doi.org/10.1088/0960-1317/20/6/064017.

[9] C.A. Schuh, C.E. Packard, A.C. Lund, Nanoindentation and contact-mode imaging at high temperatures, J. Mater. Res. 21 (2006) 725–736. https://doi.org/10.1557/jmr.2006.0080.

[10] Z.C. Duan, A.M. Hodge, High-temperature nanoindentation: New developments and ongoing challenges, JOM. 61 (2009) 32. https://doi.org/10.1007/s11837-009-0177-5.

[11] M. Conte, G. Mohanty, J.J. Schwiedrzik, J.M. Wheeler, B. Bellaton, J. Michler, N.X. Randall, Novel high temperature vacuum nanoindentation system with active surface referencing and non-contact heating for measurements up to 800 °C, Rev. Sci. Instrum. 90 (2019) 045105. https://doi.org/10.1063/1.5029873.

[12] A. Barnoush, H. Vehoff, Electrochemical nanoindentation: A new approach to probe hydrogen/deformation interaction, Scr. Mater. 55 (2006) 195–198. https://doi.org/10.1016/j.scriptamat.2006.03.041.

[13] D.R. Clarke, M.C. Kroll, P.D. Kirchner, R.F. Cook, B.J. Hockey, Amorphization and Conductivity of Silicon and Germanium Induced by Indentation, Phys. Rev. Lett. 60 (1988) 2156–2159. https://doi.org/10.1103/PhysRevLett.60.2156.

[14] G.M. Pharr, W.C. Oliver, R.F. Cook, P.D. Kirchner, M.C. Kroll, T.R. Dinger, D.R. Clarke, Electrical resistance of metallic contacts on silicon and germanium during indentation, J. Mater. Res. 7 (1992) 961–972. https://doi.org/10.1557/JMR.1992.0961.

[15] A.B. Mann, D. van Heerden, J.B. Pethica, T.P. Weihs, Size-dependent phase transformations during point loading of silicon, J. Mater. Res. 15 (2000) 1754–1758. https://doi.org/10.1557/JMR.2000.0253.

[16] A.B. Mann, D. van Heerden, J.B. Pethica, P. Bowes, T.P. Weihs, Contact resistance and phase transformations during nanoindentation of silicon, Philos. Mag. A. 82 (2002) 1921–1929. https://doi.org/10.1080/01418610208235704.

[17] J.E. Bradby, J.S. Williams, M.V. Swain, In situ electrical characterization of phase transformations in Si during indentation, Phys. Rev. B. 67 (2003) 085205. https://doi.org/10.1103/PhysRevB.67.085205.

[18] S. Ruffell, J.E. Bradby, J.S. Williams, O.L. Warren, An in situ electrical measurement technique via a conducting diamond tip for nanoindentation in silicon, J. Mater. Res. 22 (2007) 578–586. https://doi.org/10.1557/jmr.2007.0100.

[19] S. Ruffell, J.E. Bradby, N. Fujisawa, J.S. Williams, Identification of nanoindentation-induced phase changes in silicon by in situ electrical characterization, J. Appl. Phys. 101 (2007) 083531. https://doi.org/10.1063/1.2724803.

[20] J.B. Pethica, D. Tabor, Contact of characterised metal surfaces at very low loads: Deformation and adhesion, Surf Sci. 89 (1979) 182–190. https://doi.org/10.1016/0039-6028(79)90606-X.

[21] D.D. Stauffer, R.C. Major, D. Vodnick, J.H. Thomas, J. Parker, M. Manno, C. Leighton, W.W. Gerberich, Plastic response of the native oxide on Cr and Al thin films from in situ conductive nanoindentation, J. Mater. Res. 27 (2012) 685–693. https://doi.org/10.1557/jmr.2011.432.

[22] H.H. Nguyen, P.J. Wei, J.F. Lin, Electric contact resistance for monitoring nanoindentation-induced delamination, Adv. Nat. Sci: Nanosci. Nanotechnol. 2 (2011) 015007. https://doi.org/10.1088/2043-6262/2/1/015007.

[23] A. Rar, G.M. Pharr, W.C. Oliver, E. Karapetian, S.V. Kalinin, Piezoelectric nanoindentation, J. Mater. Res. 21 (2006) 552–556. https://doi.org/10.1557/jmr.2006.0081.

[24] H. Nili, G. Cheng, T.A. Venkatesh, S. Sriram, M. Bhaskaran, Correlation between nanomechanical and piezoelectric properties of thin films: An experimental and finite element study, Mater. Lett. 90 (2013) 148–151. https://doi.org/10.1016/j.matlet.2012.09.036.

[25] P. Duvivier, V. Mandrillon, K. Inal, C. Dieppedale, S. Deldon-Martoscia, J. Polizzi, Time Dependence Investigation of the Electrical Resistance of Au / Au Thin Film Micro Contacts, in: 2010 IEEE 56th Holm Conference on Electrical Contacts, 2010: pp. 1–7. https://doi.org/10.1109/HOLM.2010.5619563.

[26] S. Comby-Dassonneville, F. Volpi, M. Verdier, Electrically-functionalised nanoindenter dedicated to local capacitive measurements: Experimental set-up and data-processing procedure for quantitative analysis, Sens. Actuators, A. 294 (2019) 185–193. https://doi.org/10.1016/j.sna.2019.05.032.

[27] H. Zhou, Y. Pei, Y. Wang, H. Lei, Method to tune electrical impedance of LSMO/PMN-PT by nanocontact, Mater. Res. Express. 5 (2018) 015001. https://doi.org/10.1088/2053-1591/aa9fd6.

[28] L. Fang, C.L. Muhlstein, J.G. Collins, A.L. Romasco, L.H. Friedman, Continuous electrical in situ contact area measurement during instrumented indentation, J. Mater. Res. 23 (2008) 2480–2485. https://doi.org/10.1557/jmr.2008.0298.

[29] B. Poon, D. Rittel, G. Ravichandran, An analysis of nanoindentation in elasto-plastic solids, Int. J. Solids Struct. 45 (2008) 6399–6415. https://doi.org/10.1016/j.ijsolstr.2008.08.016.

[30] [D.J. Sprouster, S. Ruffell, J.E. Bradby, D.D. Stauffer, R.C. Major, O.L. Warren, J.S. Williams, Quantitative electromechanical characterization of materials using conductive ceramic tips, Acta Mater. 71 (2014) 153–163. https://doi.org/10.1016/j.actamat.2014.02.028.

[31] H. Nili, S. Walia, M. Bhaskaran, S. Sriram, Nanoscale electro-mechanical dynamics of nano-crystalline platinum thin films: An in situ electrical nanoindentation study, J. Appl. Phys. 116 (2014) 163504. https://doi.org/10.1063/1.4899194.

[32] G. Singh, R.L. Narayan, A.M. Asiri, U. Ramamurty, Discrete drops in the electrical contact resistance during nanoindentation of a bulk metallic glass, Appl. Phys. Lett. 108 (2016) 181903. https://doi.org/10.1063/1.4948540.

[33] S. Comby-Dassonneville, F. Volpi, G. Parry, M. Verdier, Resistive-nanoindentation: contact area monitoring by real-time electrical contact resistance measurement, MRS Comm. 9 (2019) 1008–1014. https://doi-org/10.1557/mrc.2019.74

[34] M. Bhaskaran, S. Sriram, S. Ruffell, A. Mitchell, Nanoscale Characterization of Energy Generation from Piezoelectric Thin Films, Adv. Funct. Mater. 21 (2011) 2251–2257. https://doi.org/10.1002/adfm.201002663.

[35] F. Volpi, M. Rusinowicz, S. Comby-Dassonneville, G. Parry, C. Boujrouf, M. Braccini, D. Pellerin, M. Verdier, Resistive-nanoindentation on gold: Experiments and modeling of the electrical contact resistance, Rev. Sci. Instrum. 92 (2021) 035102. https://doi.org/10.1063/5.0032682.

[36] M. Huang, T.A. Pascal, H. Kim, W.A. Goddard, J.R. Greer, Electronic−Mechanical Coupling in Graphene from in situ Nanoindentation Experiments and Multiscale Atomistic Simulations, Nano Lett. 11 (2011) 1241–1246. https://doi.org/10.1021/nl104227t.

[37] T. Kondo, J. Toyoizumi, M. Onuma, T. Shimizu, S. Kawabata, N. Watanabe, K. Mori, Investigation of electrical contacts on a nanometer scale using a Nano-manipulator in Scanning Electron Microscope, in: 2015 IEEE 61st Holm Conference on Electrical Contacts, 2015: pp. 262–265. https://doi.org/10.1109/HOLM.2015.7355107.

[38] S. Comby-Dassonneville, F. Volpi, C. Boujrouf, G. Parry, M. Braccini, S. Iruela, A. Antoni-Zdziobeka, Y. Champion, M. Verdier, F. Charlot, R. Martin, F. Roussel-Dherbey, L. Maniguet, D. Pellerin, Development and Application of a Multifunctional Nanoindenter: Coupling to Electrical Measurements and Integration In-Situ in a Scanning Electron Microscope, in: 2019 IEEE Holm Conference on Electrical Contacts, 2019: pp. 1–8. https://doi.org/10.1109/HOLM.2019.8923946.

[39] F. Houzé, R. Meyer, O. Schneegans, L. Boyer, Imaging the local electrical properties of metal surfaces by atomic force microscopy with conducting probes, Appl. Phys. Lett. 69 (1996) 1975–1977. https://doi.org/10.1063/1.117179.

[40] M. Chubarov, F. Mercier, S. Lay, F. Charlot, A. Crisci, S. Coindeau, T. Encinas, G. Ferro, R. Reboud, R. Boichot, Growth of aluminum nitride on flat and patterned Si (111) by high temperature halide CVD, Thin Solid Films. 623 (2017) 65–71. https://doi.org/10.1016/j.tsf.2016.11.045.

[41] A.G. Aberle, Surface passivation of crystalline silicon solar cells: a review, Prog. Photovoltaics Res. Appl. 8 (2000) 473–487. https://doi.org/10.1002/1099-159X(200009/10)8:5<473::AID-PIP337>3.0.CO;2-D.

[42] M.-B. Lin, (2011). Introduction to VLSI Systems: A Logic, Circuit, and System Perspective (1st ed.). CRC Press. https://doi.org/10.1201/9781439897324

[43] J.M. Bustillo, R.T. Howe, R.S. Muller, Surface micromachining for microelectromechanical systems, Proc. IEEE. 86 (1998) 1552–1574. https://doi.org/10.1109/5.704260.

[44] T. Tekin, Review of Packaging of Optoelectronic, Photonic, and MEMS Components, IEEE J. Sel. Top. Quantum Electron. 17 (2011) 704–719. https://doi.org/10.1109/JSTQE.2011.2113171.

[45] P. Scafidi, M. Ignat, Cracking and loss of adhesion of Si3N4 and SiO2:P films deposited on Al substrates, J. Adhes. Sci. Technol. 12 (1998) 1219–1242. https://doi.org/10.1163/156856198X00407.

[46] A.E. Giannakopoulos, S. Suresh, Theory of indentation of piezoelectric materials, Acta Mater. 47 (1999) 2153–2164. https://doi.org/10.1016/S1359-6454(99)00076-2.

[47] B.T. Rodriguez, D.-J. Kim, A.I. Kingon, R.J. Nemanich, Measurement of the Effective Piezoelectric Constant of Nitride Thin Films and Heterostructures Using Scanning Force Microscopy, Mater. Res. Soc. Symp. Proc. 693 (2002) 798–803. https://doi.org/10.1557/PROC-693-I9.9.1.

[48] T. Kamohara, M. Akiyama, N. Ueno, M. Sakamoto, K. Kano, A. Teshigahara, N. Kawahara, N. Kuwano, Influence of sputtering pressure on polarity distribution of aluminum nitride thin films, Appl. Phys. Lett. 89 (2006) 243507. https://doi.org/10.1063/1.2405849.

[49] S. Sridhar, A.E. Giannakopoulos, S. Suresh, U. Ramamurty, Electrical response during indentation of piezoelectric materials: A new method for material characterization, J. Appl. Phys. 85 (1999) 380–387. https://doi.org/10.1063/1.369459.

[50] V. Koval, M.J. Reece, A.J. Bushby, Ferroelectric/ferroelastic behavior and piezoelectric response of lead zirconate titanate thin films under nanoindentation, J. Appl. Phys. 97 (2005) 074301. https://doi.org/10.1063/1.1870092.

[51] M. Algueró, A.J. Bushby, M.J. Reece, R. Poyato, J. Ricote, M.L. Calzada, L. Pardo, Stress-induced depolarization of (Pb,La)TiO3 ferroelectric thin films by nanoindentation, Appl. Phys. Lett. 79 (2001) 3830–3832. https://doi.org/10.1063/1.1418258.

[52] M.Y. Soomro, I. Hussain, N. Bano, E. Broitman, O. Nur, M. Willander, Nanoscale elastic modulus of single horizontal ZnO nanorod using nanoindentation experiment, Nano. Res. Lett. 7 (2012), 146. https://doi.org/10.1186/1556-276X-7-146.

[53] N.B. Shahjahan, Z. Hu, Effects of angular misalignment on material property characterization by nanoindentation with a cylindrical flat-tip indenter, J. Mater. Res. 32 (2017) 1456–1465. https://doi.org/10.1557/jmr.2016.478.

[54] A. Asthana, H. A. Ardakani, Y. K. Yap, R. S. Yassar, Real time observation of mechanically triggered piezoelectric current in individual ZnO nanobelts, J. Mater. Chem. C, 2 (2014) 3995. https://doi.org/10.1039/c4tc00032c.

[55] T. Zheng, J. Wu, D. Xiao, J. Zhu, Recent development in lead-free perovskite piezoelectric bulk materials, Prog. Mat. Sci. 98 (2018) 552–624. https://doi.org/10.1016/j.pmatsci.2018.06.002.

[56] C.M. Lueng, H.L.W. Chan, C. Surya, C.L. Choy, Piezoelectric coefficient of aluminum nitride and gallium nitride, J. Appl. Phys. 88 (2000) 5360–5363. https://doi.org/10.1063/1.1317244.

[57] H. Shin, J.-T. Song, Piezoelectric Coefficient Measurement of AlN Thin Films at the Nanometer Scale using Piezoresponse Force Microscopy, J. Korean Phys. Soc. 56 (2010) 580–585. https://doi.org/10.3938/jkps.56.580.

[58] F. Bernardini, V. Fiorentini, D. Vanderbilt, Spontaneous polarization and piezoelectric constants of III-V nitrides, Phys. Rev. B. 56 (1997) R10024–R10027. https://doi.org/10.1103/PhysRevB.56.R10024.

[59] W. Sha, J. Zhang, S. Tan, X. Luo, W. Hu, III-nitride piezotronic/piezo-phototronic materials and devices, J. Phys. D: Appl. Phys. 52 (2019) 213003. https://doi.org/10.1088/1361-6463/ab04d6.

[60] S. Goel, B. Kumar, A review on piezo-/ferro-electric properties of morphologically diverse ZnO nanostructures, J. Alloys Compd. 816 (2020) 152491. https://doi.org/10.1016/j.jallcom.2019.152491.

[61] A. Zaszczynska, P. Sajkiewicz, A. Gradys, Piezoelectric Scaffolds as Smart Materials for Neural Tissue Engineering, Polymers 12 (2020) 161. https://doi.org/doi:10.3390/polym12010161.

[62] S.V. Anandhan, U.M. Krishnan, Boron nitride nanotube scaffolds: emergence of a new era in regenerative medicine, Biomed. Mater. 16 (2021) 044105, https://doi.org/10.1088/1748-605X/abf27d.

[63] J. Seo, A review on chemical and mechanical phenomena at the wafer interface during chemical mechanical planarization, J. Mater. Res. 36 (2021) 235–257. https://doi.org/10.1557/s43578-020-00060-x.

[64] A.K. Sinha, H.J. Levinstein, T.E. Smith, Thermal stresses and cracking resistance of dielectric films (SiN, Si3N4, and SiO2) on Si substrates, J. Appl. Phys. 49 (1978) 2423–2426. https://doi.org/10.1063/1.325084.

[65] J.W. Evans, J.Y. Evans, P. Lall, S.L. Cornford, Thermomechanical failures in microelectronic interconnects, Microelectron. Reliab. 38 (1998) 523–529. https://doi.org/10.1016/S0026-2714(97)00226-6.

[66] S. Raghavan, I. Schmadlak, G. Leal, S.K. Sitaraman, Mixed-mode cohesive zone parameters for sub-micron scale stacked layers to predict microelectronic device reliability, Eng. Fract. Mech. 153 (2016) 259–277. https://doi.org/10.1016/j.engfracmech.2015.12.013.

[67] S.J. Bull, Nanoindentation of coatings. J. Physics D: Applied Physics 38 (2005) R393–R413. https://doi.org/10.1088/0022-3727/38/24/R01.

[68] A. Yeo, Y.S. Chan, F. Che, M. Liu, K. Zhou, A combined experimental and modelling study of indentation damage test on thin-film stacked structures, Thin Solid Films. 615 (2016) 74–83. https://doi.org/10.1016/j.tsf.2016.06.052.

[69] Z. Wang, X. Zhong, L. Jiang, F. Qi, X. Ouyang, J. Wang, B. Liao, J. Luo, Effect of interfacial delamination on coating crack in thick diamond-like carbon coatings under indentation, Acta Mech. Sin. 36 (2020) 524–535. https://doi.org/10.1007/s10409-020-00930-x.

[70] M. Parlinska-Wojtan, S. Meier, J. Patscheider, Transmission electron microscopy characterization of TiN/SiNx multilayered coatings plastically deformed by nanoindentation, Thin Solid Films. 518 (2010) 4890–4897. https://doi.org/10.1016/j.tsf.2010.02.064.

[71] Y. Gaillard, C. Tromas, J. Woirgard, Pop-in phenomenon in MgO and LiF: observation of dislocation structures, Phil. Mag. Lett. 83 (2003) 553–561. https://doi.org/10.1080/09500830310001594273.

[72] J.E. Bradby, J.S. Williams, J. Wong-Leung, M.V. Swain, P. Munroe, Nanoindentation-induced deformation of Ge, App. Phys. Lett. 80 (2002) 2651–2653. http://dx.doi.org/10.1063/1.1469660.

[73] S.R. Jian, G.J. Chen, W.M. Hsu, Mechanical Properties of Cu2O Thin Films by Nanoindentation, Materials 6 (2013) 4505–4513. https://doi.org/10.3390/ma6104505.

[74] X. Li, D. Diao, B. Bhushan, Fracture mechanisms of thin amorphous carbon films in nanoindentation, Acta Mat. 45 (1997) 4453–4461. http://dx.doi.org/10.1016/S1359-6454(97)00143-2.

[75] D. Morris, S. Myers, R. Cook, Sharp probes of varying acuity: Instrumented indentation and fracture behavior, J. of Mater. Res. 19 (2004) 165-175. https://doi.org/10.1557/jmr.2004.19.1.165.

[76] R.J Nay, O.L Warren, D Yang, T.J Wyrobek, Mechanical characterization of low-k dielectric materials using nanoindentation, Microelec. Eng. 75 (2004) 103-110. https://doi.org/10.1016/j.mee.2004.01.043.

[77] M. Fujikane, S. Nagao, X.W. Liu, D. Chrobak, A. Lehto, S. Yamanaka, R. Nowak, Evaluation of carbon-doped low-k multilayer structure by nanoindentation, J. Alloys Compd. 448 (2008) 293-297. https://doi.org/10.1016/j.jallcom.2006.10.089.

[78] K. Singh, S. Sharma, S. Shriwastava, P. Singla, M. Gupta, C.C. Tripathi, Significance of nano-materials, designs consideration and fabrication techniques on performances of strain sensors - A review, Mat. Sc. in Semicond. Proc. 123 (2021) 105581. https://doi.org/10.1016/j.mssp.2020.105581.

[79] K. Vanstreels, I. Ciofi, Y. Barbarin, M. Baklanov, Influence of porosity on dielectric breakdown of ultralow-k dielectrics, J. Vac. Sci. Technol. B 31, 050604 (2013). https://doi.org/10.1116/1.4818128.

[80] C. Wu, Y. Li, A. Leśniewska, O. Varela Pedreira, J.-F. de Marneffe, I. Ciofi, P. Verdonck, M. R. Baklanov, J. Bömmels, I. De Wolf, Zs. Tőkei, K. Croes, Correlation between stress-

induced leakage current and dielectric degradation in ultraporous SiOCH low-k materials, J. Appl. Phys. 118 (2015) 164101. https://doi.org/10.1063/1.4934520.

[81] S. Postorino, D. Grassano, M. D'Alessandro, A. Pianetti, O. Pulci, M. Palummo, Strain-induced effects on the electronic properties of 2D materials, Nanomat. and Nanotech. 10 (2020) 1–11. https://doi.org/10.1177/1847980420902569.

[82] C. Wang, K. Xia, H. Wang, X. Liang, Z. Yin, Y. Zhang, Advanced Carbon for Flexible and Wearable Electronics, Adv. Mater. 31 (2019) 1801072. https://doi.org/10.1002/adma.201801072.

[83] A. Vidana, S. Almeida, M. Martinez, E. Acosta, J. Mireles Jr., T. –J. King, D. Zubia, Exponential Conductivity Increase in Strained MoS2 via MEMS Actuation, MRS Advances 4 (2019) (38-39), 2135-2142. https://doi.org/10.1557/adv.2019.282.

[84] D. Tan, C. Jiang, Q. Li, S. Bi, J. Song, Silver nanowire networks with preparations and applications: a review, J. of Mater. Sc. : Mater. in Elec. 31 (2020) 15669–15696. https://doi.org/10.1007/s10854-020-04131-x.

[85] M.-W. Kim, M.L. Lifson, G.A. Rebecca, J.R. Greer, B.-J. Kim, Recoverable Electrical Breakdown Strength and Dielectric Constant in Ultralow-k Nanolattice Capacitors, Nano Lett. 19 (2019) 5689−5696. https://doi.org/10.1021/acs.nanolett.9b02282.

[86] S. Rossi, F. Russo ,M. Calovi, Durability of vitreous enamel coatings and their resistance to abrasion, chemicals, and corrosion: a review, J. Coat. Technol. Res., 18 (2021) 39–52. https://doi.org/10.1007/s11998-020-00415-3.